

Design and Comparison of Diamond- and Sapphire-Based NbN KIDs for Fusion Plasma Polarimetric Diagnostics

Francesco Mazzocchi,* Konstantin Ilin, Sebastian Kempf, Artem Kuzmin, Dirk Strauß, and Theo Scherer

Design and characterization measurements performed on kinetic inductance detectors (KIDs) produced on sapphire and polycrystalline diamond substrates are presented. Designed as part of a nuclear fusion polarimetric diagnostic, the foreseen plasma-probing frequency of the final devices is 1.3 THz with a maximum response time under 10 ms and cross-polarization target accuracy of 1%. These detectors are based on superconducting micro-resonators that undergo detuning upon absorption of radiation. The main characteristics of the devices include polarization sensitiveness and lumped-elements multi-pixel configuration produced from photo-lithographed niobium nitride (NbN) thin films. The direct current (DC) and microwave characterization measurements highlight large differences in the thin film quality, with the superconductor deposited on diamond showing reduced critical temperature, lower critical current density, and increased values of the kinetic inductance. This difference is likely due to the higher lattice constant and thermal expansion coefficient mismatch between film and substrate in the case of diamond, with the different surface finish quality of the crystalline samples available also playing a role. The devices on both substrates show a bolometric response to THz radiation that fulfills the requirement guidelines and represent a good starting point to optimize the design for the application at hand.


their resonant properties when under radiation load. Incoming photons break down Cooper pairs, resulting in a rise of the kinetic inductance of the circuits and, therefore, a shift of their resonance frequency and phase. This shift can be measured as a change in the transmission-scattering parameter S_{21} through common radio-frequency division multiplexing (FDM) techniques. Lumped elements KIDs (LEKIDs) are particularly attractive because the resonator's inductor is designed to also serve as the radiation absorber. Given the aforementioned properties, KIDs represent a promising candidate as polarimetric diagnostic for nuclear fusion facilities. Their main advantages over other kind of detectors include a very simple, single-layer structure that can be realized with conventional photolithographic techniques, fast action, and FDM readout. Thanks to these characteristics, the final instrument can be realized with a very limited footprint, enabling the implementation of multiple line-of-sight configurations. KIDs can be also designed to be polarization sensitive,

1. Introduction

Kinetic inductance detectors (KIDs) have proven themselves as a very capable cryogenic detector technology with applications in various fields, including astrophysics^[1–3] and imaging.^[4] They are characterized by flexibility of design, high sensitivity, and ease of production. KIDs consist of inductance–capacitance (LC) superconducting micro-resonators that show variations of

in which case only one detector is necessary and both the mechanical polarization status modulator and selection stage can be removed. This additionally simplifies the final instrument optical scheme and improves reliability.^[5] Polarimetry is a well-established technique employed to monitor fundamental plasma parameters like the plasma current density.^[6–8] We recently proposed a polarimetric instrument based on a 1.3 THz quantum cascade lasers (QCLs)-probing source for application in future

F. Mazzocchi, D. Strauß, T. Scherer
Institute Of Applied Materials - Applied Materials Physics
Karlsruhe Institute of Technology (KIT IAM-AWP)
Campus Nord, 76344 Eggenstein Leopoldshafen, Germany
E-mail: francesco.mazzocchi@kit.edu

 The ORCID identification number(s) for the author(s) of this article can be found under <https://doi.org/10.1002/pssa.202200271>.

© 2022 The Authors. *physica status solidi (a) applications and materials science* published by Wiley-VCH GmbH. This is an open access article under the terms of the Creative Commons Attribution-NonCommercial-NoDerivs License, which permits use and distribution in any medium, provided the original work is properly cited, the use is non-commercial and no modifications or adaptations are made.

DOI: 10.1002/pssa.202200271

K. Ilin, S. Kempf
Institute of Micro- and Nano-electric Systems
Karlsruhe Institute of Technology (KIT IMS)
Campus West, 76187 Karlsruhe, Germany

A. Kuzmin
Laboratory for Applications of Synchrotron Radiation
Karlsruhe Institute of Technology (KIT IAS)
Campus South, 76131 Karlsruhe, Germany

nuclear fusion facilities.^[9] We therefore decided to start experimenting with a polarization-sensitive iteration of these detectors, with the first prototypes fabricated onto a high resistivity silicon (HRSi) substrate.^[5] While HRSi is a proven material for this kind of technology, it is nevertheless sensitive to radiation damage^[10] that can occur in environments potentially flooded with highly energetic radiation as is the case when in close proximity to a tokamak reactor. We therefore decided to explore the use of sapphire and diamond as alternative materials, with substrate thicknesses of 330 and 700 μm , respectively. These media have outstanding mechanical and optical characteristics and, in the case of diamond, also very good radiation hardness and thermal conductivity. Sapphire is also a widely studied substrate for NbN thin-film detectors with a rich literature^[11,12] and well-established deposition processes for high-quality thin films and will represent a performance benchmark for the detectors obtained on polycrystalline diamond.

2. Detector Design and Modeling

Each detector unit is made up by four resonators, arranged in a crossed configuration, rotated by 90° with respect to its neighbors (Figure 1). Each pixel is composed by two distinct parts, a $1 \times 1 \text{ mm}^2$ inductor (meandering, continuous line) and an interdigital capacitor (IDC). All the NbN tracks composing the resonators are $10 \mu\text{m}$ wide with a $40 \mu\text{m}$ separation between two adjacent inductor lines and a thin-film thickness of 15 nm . While the inductor is common for all the pixels, the number and length of the IDC fingers are variable, to tune each resonator to its own resonance frequency and enable FDM readout. Figure 2 represents the current density inside one of the pixels at its resonance frequency. It is apparent that its value is constant on the whole inductive area, while lower levels are associated to detuning of the resonator due to a pair breaking event independent from where that event takes place. This has the advantage of not having to direct the detectable photons to a specific point on the



Figure 1. The 2D model of a complete detector unit, including the microstrip feed-line.

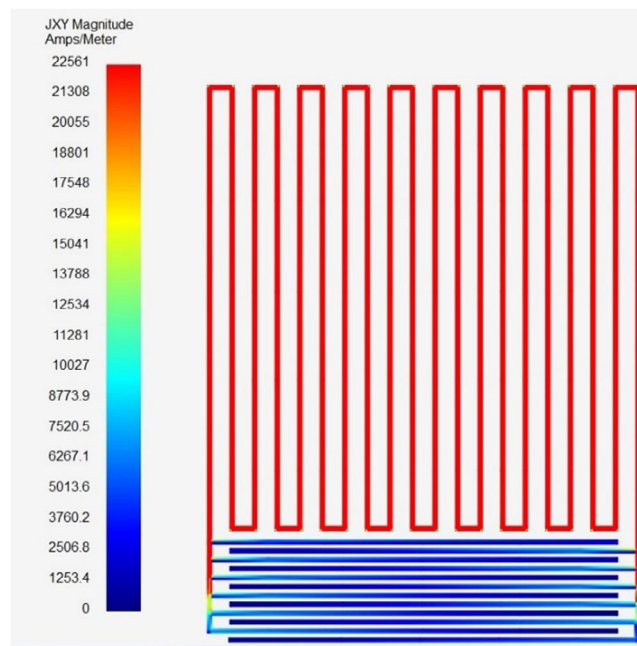


Figure 2. Simulation of current induced in one of the pixels at its resonance frequency.

resonator to maximize the response, allowing them to fall naturally onto it.^[13] The much lower values of current density present in the capacitor also mean that we don't expect it to significantly contribute to the detection of radiation. The polarization selectivity is given by the geometrical design of the unit, that greatly favors absorption of waves polarized parallel to the long sides of the inductor. As already mentioned, KIDs are micro-resonators with characteristic frequency $\omega = 1/\sqrt{LC}$, where the total inductance $L = L_m + L_k$ is given by a geometrical part L_m and a kinetic one L_k , deriving from the inertia of the charge carriers. The circuits are characterized by an intrinsic quality factor $Q_0 = \omega/\Delta\omega$, where $\Delta\omega$ is the half-power bandwidth of the resonance dip. This quantity represents a measure of the ratio between the energy stored in the resonator and the energy lost at each oscillation cycle. For a complete device, where both resonators and a readout line are present, we need to consider the total quality factor $1/Q_T = (1/Q_0 + 1/Q_C)$ with Q_C being the quality factor associated to the coupling between the pixels and the micro-strip used to excite and read them. Strong coupling corresponds to low values of the associated quality factor when compared to Q_0 , resulting in Q_C dominating Q_T , leading to wide resonance dips.^[14] Being able to tune these characteristics is of the utmost importance: two adjacent resonances having widths larger than their relative separation would lead to partial overlap of signals from two different pixels. Additionally, the photo-generated quasi-particles lead to a decrease of the internal quality factors and we expect their value, revealed by preliminary simulations with Sonnet Software^[15] to be in the 10^3 – 10^6 range, to drop to around 10^3 – 10^4 ^[16] once illuminated by the source. It is important to design the coupling quality factor to be within a similar values range as the loaded one, given that the sensitivity of the detector is in this way boosted.^[17]

3. Thin-Film Deposition, Patterning, and DC Characterization

The deposition process has been performed in a direct current (DC) reactive magnetron sputtering chamber equipped with a niobium target. We first carried out a warm-up and a pre-cleaning of the target surface in a pure argon atmosphere at a pressure of 1.8×10^{-3} mbar. We then added nitrogen, reaching a pressure of 2.1×10^{-3} mbar and, given a deposition rate of 0.065 nm s^{-1} as experimentally determined in previous activities, a 15 nm thick NbN film was obtained with 3 min and 50 s of deposition time. Substrate temperatures during the process were $850 \text{ }^\circ\text{C}$ for sapphire and $750 \text{ }^\circ\text{C}$ for diamond. The lower temperature of the second deposition was set to decrease the risk of degrading the substrate.^[18] The patterning was done through UV photolithography. The reactive ion etching (RIE) was performed in a $\text{SF}_6 + \text{O}_2$ atmosphere, with gas flows of 30 and 6 sccm, respectively, at a pressure of roughly 350 mbar. We then proceeded with the first characterization measurements of the deposited films by recording the resistance–temperature (R – T) and current–voltage (I – V) curves. The data was collected with the use of a dipstick slowly immersed into a liquid He dewar at an approximate cooling rate of 0.2 K s^{-1} . From **Figure 3**, it's evident that the quality of the deposited superconducting film onto the sapphire substrate is higher than the one on diamond. As result, the film deposited onto sapphire has a $T_C = 13.5 \text{ K}$, and a very sharp transition with $\Delta T_C = 0.2 \text{ K}$, whereas diamond shows a T_C equal to 9.05 K and ΔT_C of 1.2 K . The kinetic inductance was then estimated with the expression taken from the works of Annunziata et al.^[19] and Mauskopf et al.,^[20] equal to

$$L_k = \frac{\hbar R_s}{\pi \Delta} \quad (1)$$

with R_s representing the sheet resistance. Values of R_s at 20 K used for the calculations were roughly 70 for the films deposited on sapphire and 175 for the films on the diamond substrate,

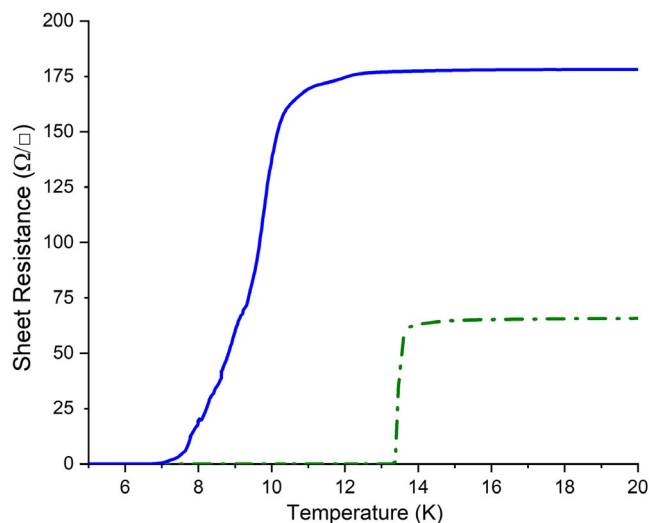


Figure 3. R – T curves of niobium nitride (NbN) films deposited onto sapphire (green, dashed–dotted) and diamond (blue, continuous) substrates.

resulting in calculated L_k values of 7.3 and $22.7 \text{ pH } \square^{-1}$ respectively. The I – V measurements performed at 4.2 K confirm what emerged from the R – T curves, with a critical current density of $9.3 \times 10^6 \text{ A cm}^{-2}$ for the films on sapphire and 5.67×10^5 obtained on diamond. There are a number of possible reasons that may lead to this apparent difference in film quality, with lattice mismatch likely having the biggest influence. Sapphire has a lattice parameter a equal to 4.785 \AA ,^[21] representing a better match for the NbN unit cell ($a = 4.446 \text{ \AA}$) than diamond ($a = 3.567 \text{ \AA}$). The lattice mismatch induces mechanical stresses in the thin films, worsening its uniformity and leading to lower critical temperatures and wider transitions. The mismatch is present also in the low-temperature thermal expansion coefficients for the three materials, with sapphire and NbN having very close values (around $7\text{--}8 \times 10^{-1} \text{ K}^{-1}$ ^[22,23]) while diamond presents a lower value around $2\text{--}5 \times 10^{-9} \text{ K}^{-1}$.^[24] The additional stresses arising during the cooldown phase can result in further degradation of the superconductor. Interdiffusion and film–substrate interface reactions may also be present, contributing to the the weakening of the superconductivity. Additionally, while the sapphire and silicon monocrystalline substrates were subject to surface optimization for epitaxial growth with an extremely low roughness ($\leq 3 \text{ \AA}$), the diamond substrates received standard polishing only, leading to roughness values around 5 nm . Finally, granularity of the diamond substrates, with crystals in the micrometer dimension, may have influenced the quality of the deposited thin films. Observations performed with an optical microscope following the cooldown phase (**Figure 4**) show a highly irregular film on diamond, in stark contrast with the one deposited onto sapphire. These considerations notwithstanding, the film on diamond didn't show any flaking over time, sign of a good adhesion to the substrate.

4. Simulations

To validate the design and investigate the occurrence of detrimental phenomena like cross talk, we performed extensive simulations of single-, dual-, and quadruple-pixel systems. Although sapphire is naturally birefringent, we nevertheless used an isotropic model, since our substrate samples were all R-cut and could be modeled with the use of an effective ϵ_r with a value of 10.06 , while for the diamond the value was set to 5.67 . The loss tangent was set equal to 5×10^{-6} for sapphire and 10^{-5} for polycrystalline chemical-vapor-deposition (CVD) diamond.^[25,26] The substrate thicknesses at our disposal were $330 \text{ }\mu\text{m}$ for sapphire and $700 \text{ }\mu\text{m}$ for diamond. The feed-lines were sized to obtain $50 \text{ }\Omega$ impedance, matching the electronics readout. The other material-related parameter used as input in the simulation was the value of L_k obtained as described in Section 3.

The first aspect we focused on was finding a wide range of pixel resonance frequencies. Leaving the inductive part untouched, we varied the number of IDC fingers (10, 11, and 12) and their length, from 700 to $900 \text{ }\mu\text{m}$ in $10 \text{ }\mu\text{m}$ steps. The results of the simulations shown in **Figure 5** and **6** outlined a range of frequencies from 1.25 to 1.8 GHz for the diamond substrate, and from 1.35 to 1.9 GHz for sapphire.

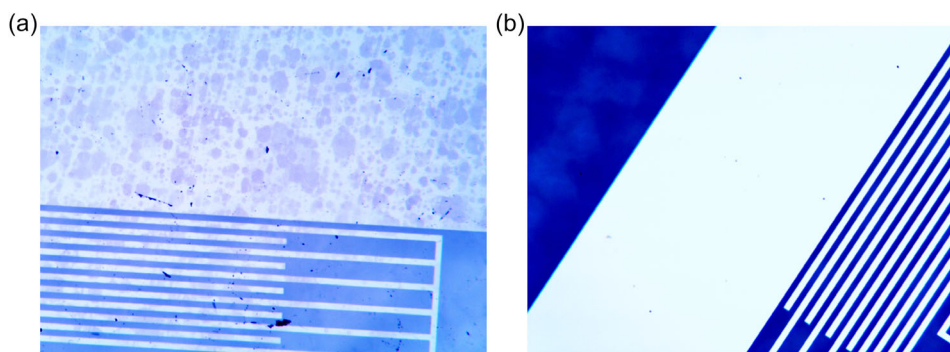


Figure 4. a,b) Optical microscopy images of NbN thin films deposited on the diamond (a) and sapphire substrates (b), taken after cooldown.

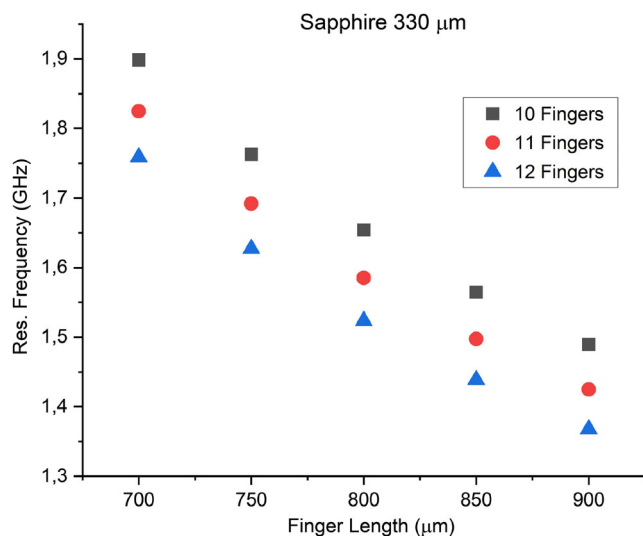


Figure 5. Simulated pixel resonance frequency for the sapphire substrate as a function of interdigital capacitor (IDC) finger number and length.

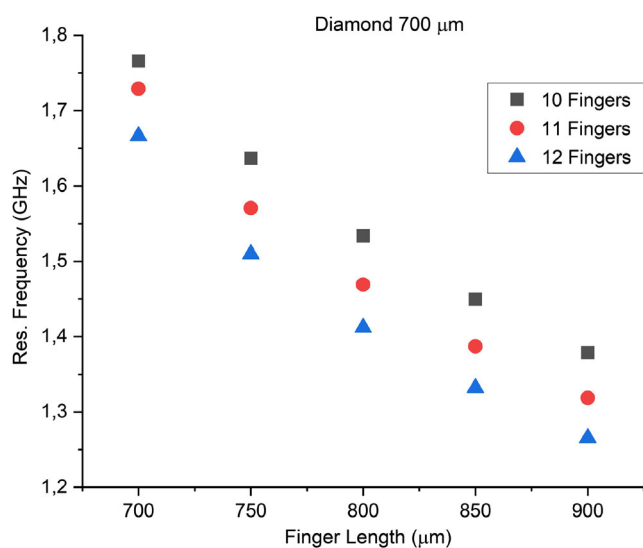


Figure 6. Simulated pixel resonance frequency for the diamond substrate as a function of IDC finger number and length.

Given the presence of only four pixels, we could choose combinations of well-spaced frequencies for the prototypes production while being reasonably sure to avoid overlap between adjacent resonances.

One of the major improvements of KIDs over competing technologies is their innate multiplexability, enabling the readout of large pixel arrays through a single (or a very small number of) transmission line. This leads to simplified design requirements and tightly packaged configurations. While this is indeed advantageous, it also demands particular attention to avoid cross talk.^[27] This phenomenon derives from parasitic coupling between neighboring pixels and manifest itself as a change of the position and shape of the resonances.^[14,28,29] To study its occurrence, we simulated two identical-pixel systems that, in the absence of cross talk, are characterized by a single (double-degenerate) resonance dip. The coupling of the two resonant modes lifts the degeneracy and splits their frequencies. The larger the separation in frequency between the newly formed resonances, the stronger the effect. The calculations were performed at different inter-pixels distances (10–100 μm in 10 μm steps), and with different shielding configurations: BARE, OPEN-BOX, and BOX (Figure 7). In the latter two, a 10 μm wide NbN strip surrounds either three or four sides of a single resonating unit.

In the case of the OPEN-BOX configuration, the capacitor side of the resonators has an unobstructed view of the microstrip. This was done to investigate the possibility of implementing shielding while keeping a good coupling between pixels and transmission line. The results are presented in Figure 8 and 9. Diamond presents lower-frequency separation between the degenerate resonances in the case of the un-shielded configuration. The values of the fractional splitting $\Delta\nu/\nu$ in this scenario at 10 μm distance are 5.8×10^{-4} and 3.9×10^{-3} for diamond and sapphire respectively and drop to 5.1×10^{-5} and 1.2×10^{-3} at 100 μm. To take into account the different substrate thicknesses, we ran an additional simulations set based on a 330 μm diamond substrate. Although the cross talk increases when compared to the 700 μm thick samples, the separation values associated with the un-shielded devices are still well below those obtained from the sapphire substrate, while shielded samples show in all cases similar performances. The additional structures of the BOX and OPENBOX configurations lead to larger frequency separation values on both substrates. This result is

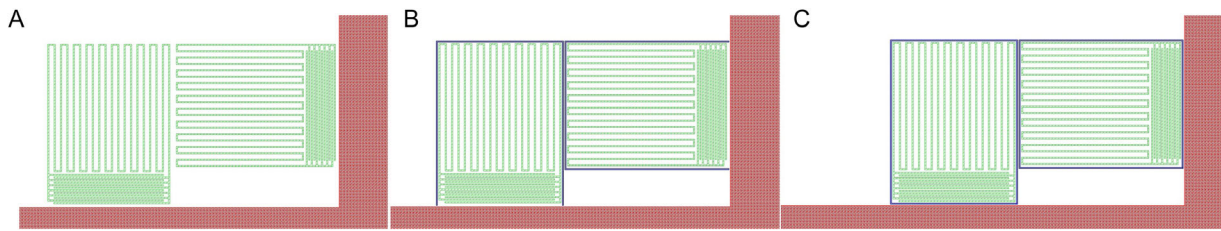


Figure 7. Sonnet model of two-pixel system used to study the occurrence of cross talk. A) The BARE configuration, B) the OPEN-BOX, and C) the BOX configuration. The resonators are in green color, the in-plane shielding structures surrounding resonators in (B,C) in blue and in red the partially visible microstrip transmission line.

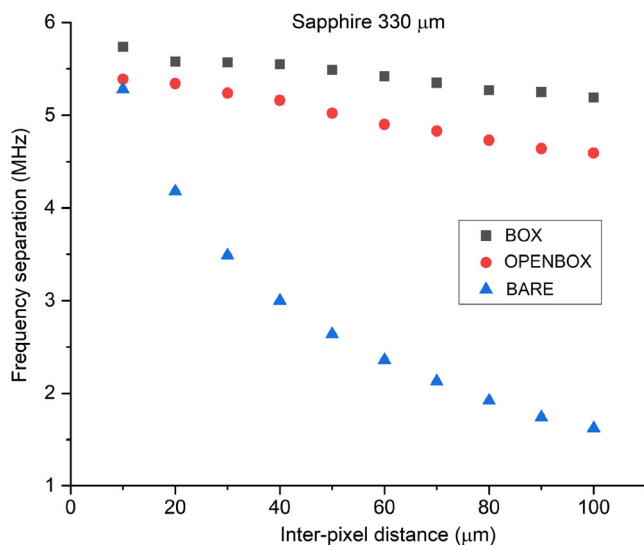


Figure 8. Frequency separation versus inter-pixel distance in case of cross talk for different shielding configurations (see Figure 7) as indicated in the legend—sapphire substrate.

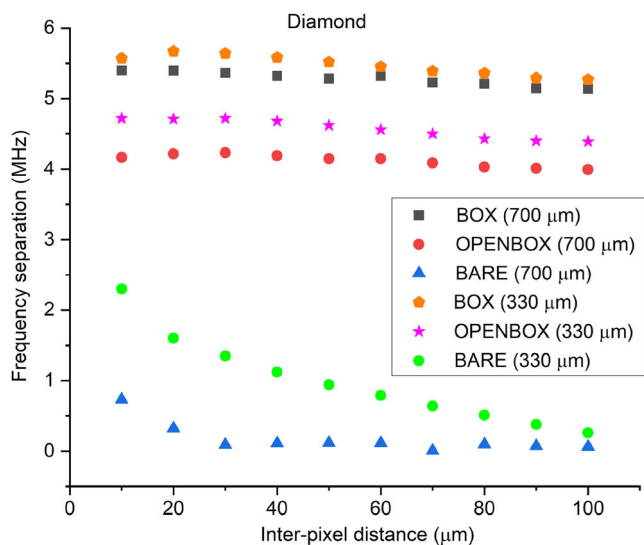


Figure 9. Frequency separation versus inter-pixel distance in case of cross talk for different shielding configurations (see Figure 7) and substrate thicknesses as indicated in the legend—diamond substrate.

in contrast with what can be found in literature,^[14,29,30] where analogous grounded structures are successfully used to limit this effect. We attribute this difference to the floating nature of the films used in our iteration of the KIDs and to their geometrical configuration. The 90° tilt of our LEKIDs array pixels translates to pixel-to-pixel coupling involving mainly the inductive parts of the resonators. In the case of the BARE pixels, the long side of the inductor interacts with the much shorter segments at the bottom of its neighbors, while the additional floating NbN strip present in the BOX and OPEN-BOX configurations end up acting as coupling booster, since it extends completely around the meandering line. Works in literature almost exclusively present same-direction-facing resonators, excited with co-planar waveguides. Increasing the pixel-to-pixel distance helps especially in the case of sapphire, but does not completely solve the problem.

To investigate the strength of the coupling between the pixels and the readout line, we simulated two-pixel models varying the distance between the transmission line and the IDC, again from 10 to 100 μm in 10 μm steps. The BARE and both shielded systems have been studied.

The results can be seen in **Figure 10** and **11**. The BOX configurations limits the coupling even for very short separation

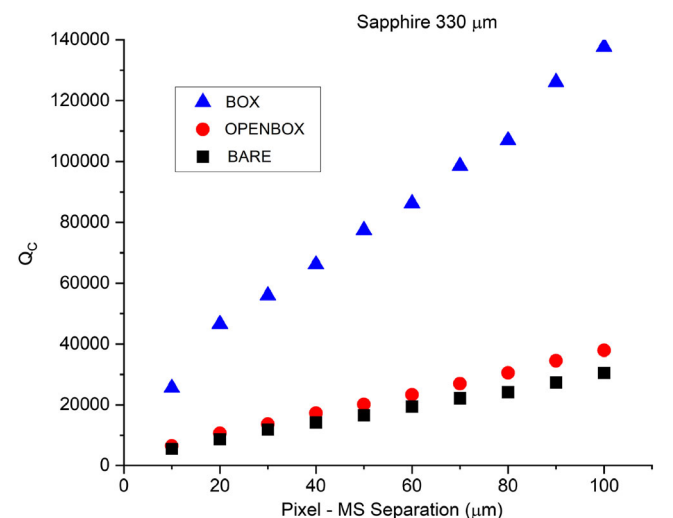


Figure 10. Coupling quality factor of the pixels over the sapphire substrates versus distance between pixel and readout microstrip as calculated from the simulations for different shielding configurations shown in Figure 7.

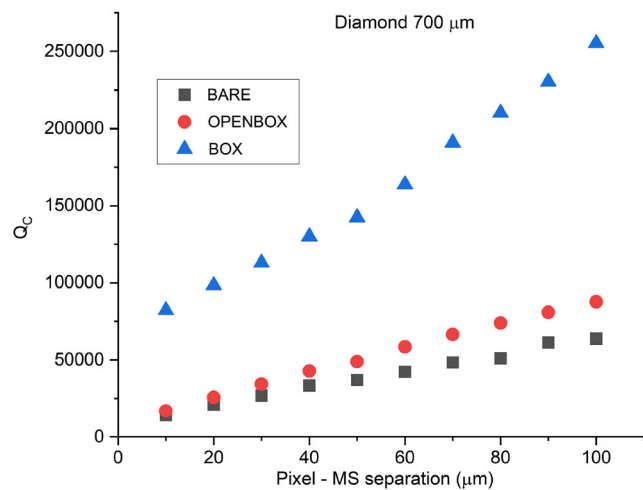


Figure 11. Coupling quality factor of the pixels over the diamond substrates versus distance between pixel and readout microstrip as calculated from the simulations for different shielding configurations shown in Figure 7.

distances, pushing the values of Q_C outside the desired range of around 10^4 . The OPEN-BOX has, as expected, a limited effect on the coupling, with values lying in the same range as the BARE ones. In any case, we should avoid placing pixels at more than 50–60 μm of distance, to limit both the coupling quality factors values and the detector footprint. Being able to pack the single resonators closely together is of high importance, since it would make beam alignment over the detector easier and less prone to successive misalignment.

The final batch of simulations computed the response to the excitation tone of the complete prototypes and are reported in the Figure 12 and 13. The purple traces represent the resonances associated to the detector model while the green,

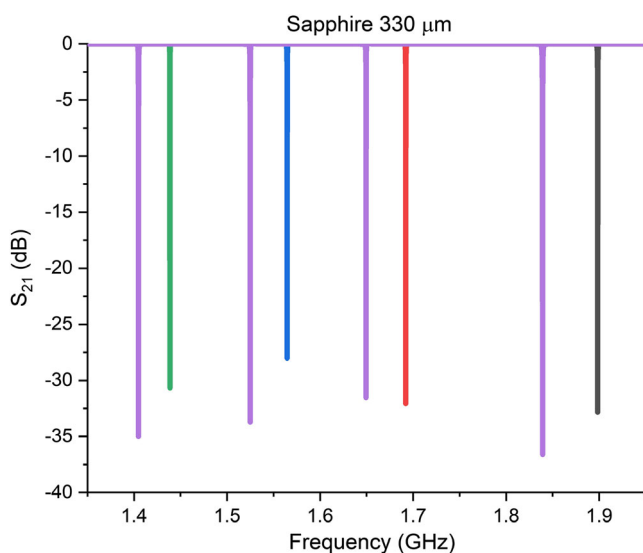


Figure 12. Simulation of one of the complete detector prototypes (purple trace), along with the correspondent single-pixel resonances (green, blue, red, and black dips)—sapphire substrate.

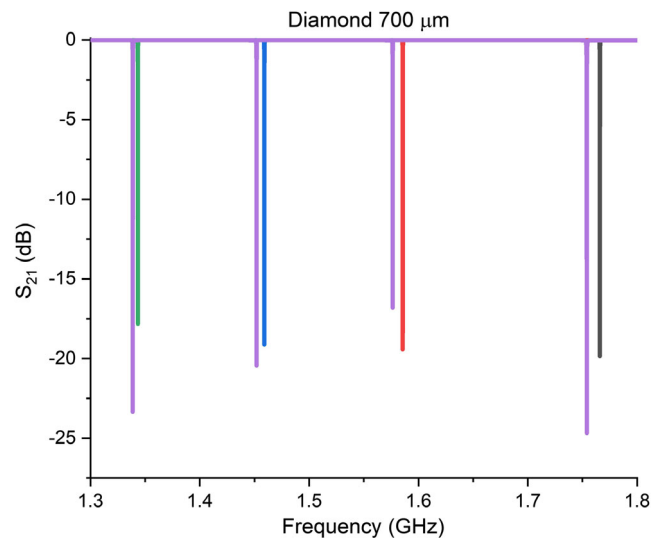


Figure 13. Simulation of one of the complete detector prototypes (purple trace), along with the correspondent single-pixel resonances (green, blue, red, and black dips)—diamond substrate.

blue, red, and black dips relate to the single resonators simulated in the frequency tuning part of this study. As it can be seen, the pixels in the prototypes oscillate with a longer period than when they are taken singularly. The KIDs couple to the ground plane via a stray capacitance that is increased by the modified geometry of the readout line of the complete detector unit, leading to lower resonance frequencies. This difference is larger for the “faster” pixels, in virtue of their lower capacitance that makes them more sensitive to this kind of effect. The lower ϵ_r of diamond helps to limit this effect also in this context. In any case, neither the sapphire nor the diamond devices show any sign of cross talk in the computed responses as evidenced by the lack of additional dips, a sign of the resonances being sufficiently apart to negate any parasitic coupling. We therefore selected for production the detectors with the smallest physical separation between pixels, equal to 10 μm , and no shielding.

5. Microwave and THz Characterization Measurements

The measurements performed to check the response of the detector to the readout tone are reported in the Figure 14 and 15, and have been carried out with a dipstick immersed in LHe and equipped, this time around, with semi-rigid SubMiniature version A (SMA) cables and adapters to connect it to a vector network analyzer (VNA). The input power of all the measurements was set at -20 dBm to avoid saturation. In the case of NbN on sapphire substrate, the ripple-like structures and the slight monotonic decreasing baseline present in the trace of Figure 14 indicates the presence of an impedance mismatch between the transmission line and the readout electronics. That being said, the resonances are quite deep and very sharp, an additional sign of the good quality of the deposited thin NbN film.

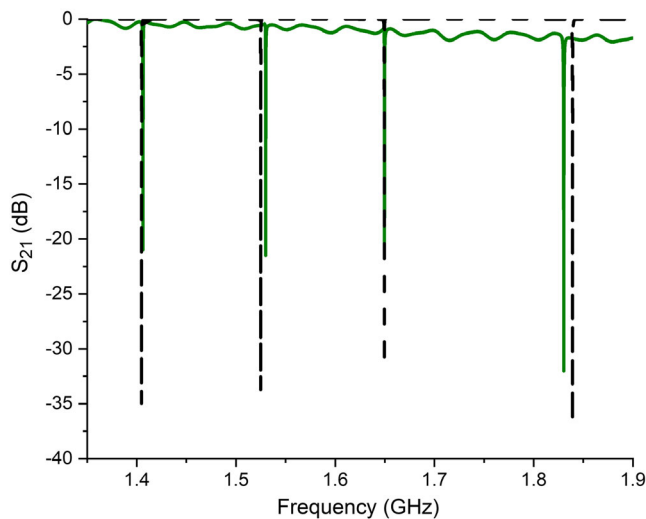


Figure 14. Measured (green) and simulated (black dashed) resonances of the prototype 1 configuration deposited on the sapphire substrate.

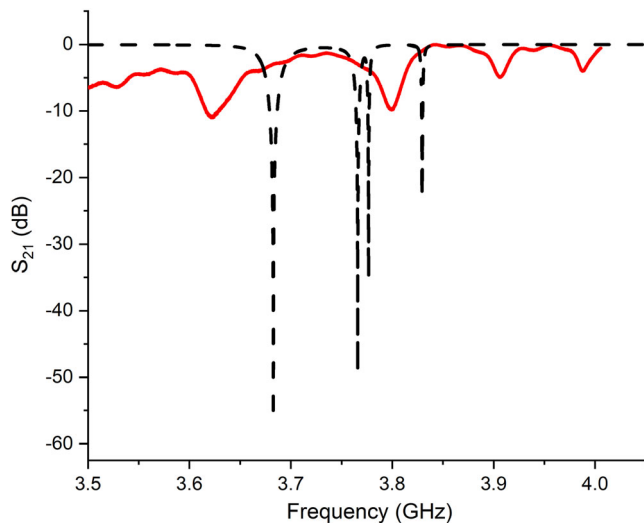


Figure 15. Measured (red) and simulated (black dashed) resonances of the prototype 3 configuration deposited on the diamond substrate.

Values of the coupling Q factors were extracted by estimating the -3 dB bandwidth and the S_{21} value of each resonator with a Lorentz fit of the measured resonance peaks and are in the 4000 range, a factor approximately 1.5 times smaller than those calculated from the simulations. The results of the measurements on the diamond substrate are quite different, as it is evident from Figure 15. From the simulations, we expected first-order resonances located roughly between 1.2 and 1.6 GHz. The relatively low T_C of the superconductors deposited on diamond leads to the presence of a substantial quantity of unpaired electrons in the films, resulting in significant ohmic losses, resulting in extremely shallow first-order resonances that end up being embedded in the baseline noise and, therefore, are undetectable. We managed nevertheless to record some higher-frequency modes roughly located between 3.5 and 4 GHz that

underwent position shift as we altered the readout power injected by the VNA, therefore excluding the possibility of them being measurement artifacts. Given the poor quality of the films deposited on diamond, the presence of these higher-frequency resonances is somehow unexpected and leads us to extend our initial set of simulations toward higher frequencies to include the band of the measurement (black dashed curve in Figure 15). The simulation revealed the presence of additional resonances located roughly between 3.7 and 3.9 GHz. From a Sonnet analysis of the current density distribution, these resonant modes are collective in nature and involve all the resonators at once, in a distributed-like fashion. Correspondence with the simulated wave forms is nevertheless poor and attributable to the highly dis-uniform nature of the deposited films. The very low values of the total quality factors associated to these dips, in the order of 10^2 , confirm the lossy nature of the resonators as also outlined by the DC characterization measurements.

Figure 16 shows the response to THz radiation produced by one of the pixels of the sapphire prototype, while in **Figure 17** the analogous measurements performed on the diamond sample is reported. The radiation source employed consisted in a backward wave oscillator (BWO) coupled to a Schottky diode frequency tripler, capable of fully tunable emission from 650 GHz up to 1.16 THz. The source was operated at 900 GHz, since it corresponds to the maximum emitted power with the tripler installed, and the emitted radiation was chopped at a frequency of 23 Hz.

The samples were inserted in a liquid helium bath cryostat, with a 10 and a 20 dB attenuators attached to port 1 of the detector block and a cryogenic low noise amplifier at port two. An additional room-temperature amplifier was inserted between the cryostat output and the VNA. With a measured THz power of $47 \mu\text{W}$ emitted right after the tripler, we estimate roughly $20 \mu\text{W}$ falling onto the resonators area after passage of the generated THz signal through quasi-optical beam delivery and the cryostat window. The response time of the resonators, that can be as low as a few nanoseconds,^[31] is associated with the resonator ring-down time $\tau = Q_T/\pi\nu$, where Q_T indicates the

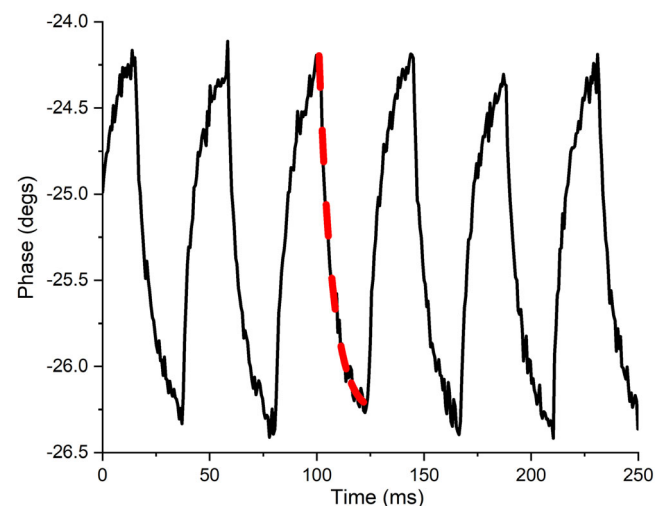


Figure 16. Phase response of one of the pixels of the prototype 1 realized on the sapphire substrate. The red dashed line indicates the exponential decay fit used to calculate the ring-down time of the resonator.

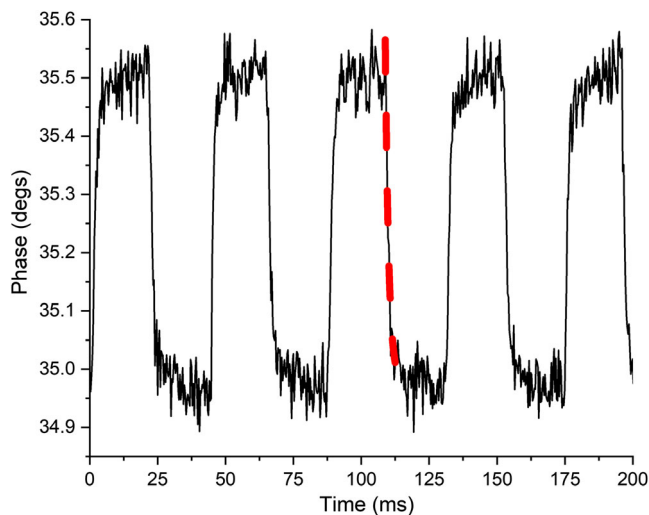


Figure 17. Phase response of one of the pixels of the prototype 3 realized on the diamond substrate. The red dashed line indicates the exponential decay fit used to calculate the ring-down time of the resonator.

total quality factor and ν is the central frequency. The measurements of the sapphire samples were performed at the temperature of 4.5 K. The phase responsivity of these devices is in the order of $0.1^\circ \mu\text{W}^{-1}$, with a response time scale in the order of 6 ms, as determined by an exponential decay fit over the recorded trace. The diamond sample was measured at a temperature of 5.5 K and presents a lower responsivity of $0.03^\circ \mu\text{W}^{-1}$ but faster response at roughly 1 ms. In both cases, the time scales measured are more in line with a bolometric regime^[32] rather than involving the direct breakdown of Cooper pairs. NbN thin films over sapphire are regularly used for hot electron bolometer mixing applications with theoretical bandwidths in excess of 10 GHz,^[33,34] limited only by the electron–phonon relaxation time. The low Kapitza resistance between substrate and film at around 4–5 K leads to very fast thermalization times, so we explain the long response times as due to the large volume of the 5×5 mm substrates used for each of the KIDs. The trace extracted from the measurements of the diamond prototype also presents a flatter, more square wave like response, indication of faster thermal dynamics. The prototypes fulfill in any case the International Thermonuclear Experimental Reactor (ITER) requirements of 10 ms of minimum time resolution.^[35]

One of the most appreciable characteristics of KIDs is their extremely low noise levels, with state-of-the-art values in the order of $10^{-1} \text{W}/\sqrt{\text{Hz}}$.^[36] The noise power density of the detectors was extracted from the measurements of the response without optical load to which an fast Fourier transform (FFT) algorithm with power normalized to the time-integral squared amplitude was applied. The relatively high values measured in our prototypes, around 10^{-8} can be attributed to the high frequency of generation–recombination events in the superconductor, result of the measurements being performed, in both cases, at relatively high temperatures. Noise levels are in any case far below the foreseen probing power of the final instrument.

Figure 18 shows the response of a single pixel of the sapphire prototype 1 to two perpendicular polarization directions of the

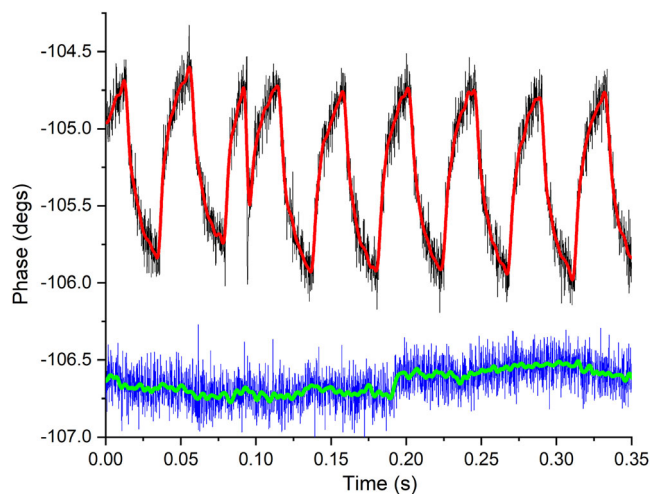


Figure 18. Phase response of one of the pixels of the prototype 1 configuration deposited on sapphire substrate to two different polarization planes. In black, the response for polarization parallel to the inductor main lines, in blue the one for the perpendicular direction. Red and green curves represent smoothing of the measured tracks by FFT shown for clarity purpose.

incoming light. The polarization selector was composed by a wire grid polarizer, preceded by a wave plate. We expected the contribution of the inductor short transverse elements to the detection of the perpendicular polarization to be negligible, given the low 25:1 ratio between the length of the main lines and the that of the segments. The resonators geometry is effective at rejecting perpendicular polarization components and therefore the concept of a polarimeter based on this design is valid. This also serves as proof that the bolometric response is given by absorption of radiation by the superconducting thin films only, since the substrates themselves are not polarization selective, and validates the choice of high-optical-quality materials as base for these devices.

6. Conclusions

We have presented the design study and first characterization measurements of an innovative KID unit with a lumped element design based on sapphire and diamond substrates, and niobium nitride superconducting thin films. The detector has been designed to be part of a polarimetric diagnostic system for nuclear fusion application, taking into consideration the guidelines specified for the upcoming ITER tokamak machine. An extensive simulation study, comprehensive of frequency tuning, estimation of the resonator–feed line coupling and occurrence of cross talk has been performed to tailor the detectors to the application at hand. We obtained similar resonance frequency ranges for the two substrate materials, with the sapphire detectors oscillating in the 1.35–1.9 GHz band, while the resonances related to the diamond ones sit in a slightly lower range between 1.25 and 1.8 GHz. Thanks to the large total bandwidth obtained with the simulations and the limited number of pixels composing the detector, the separation between the resonances was large enough to negate the occurrence of cross talk. This, united to the fact that simulations of the shielding have

shown the detrimental effect of such structures in the resonators operation, allowed us to settle for a BARE pixel design, simplifying the design and enabling a very compact packaging of the arrays. The thin-film and microwave characterization measurements outlined the great difference in quality of the superconducting thin films deposited on the two substrates, with the films on diamond believed to be suffering from lattice and thermal expansion mismatch and from a rough surface finish of the substrate. Measured response to terahertz radiation showed in both cases response times in the order of the millisecond that we attribute to the cooling of the relatively large volume substrates in a bolometric operating regime. Measurements of the response to radiation polarized along perpendicular directions validated the adopted polarimetric design and the choice of high-optical-quality materials as base for the devices. Such performances could be additionally improved by the adoption of an antenna-coupled detector configuration, at the expense of increased complexity of the deposition and patterning processes. The prototypes fulfill the response time requirements specified by ITER for a polarimetric diagnostic, and represent a good starting point for the optimization of these devices for the application at hand. Nevertheless, the response we observed needs to be better tested in the upcoming experimental activity involving a dedicated readout system. The authors plan to produce a second batch of resonators on the diamond substrate with much thicker films, to limit the influence of the proximity effect³⁷ and of the granularity of the films, and obtain critical temperatures closer to those of bulk NbN. The use of a dielectric buffer layer like aluminum nitride and epitaxially grown single-crystalline diamond substrates could also represent a viable solution to greatly improve the performances of devices based on this innovative material and will be the subject of additional investigation in the near future.

Acknowledgements

Open Access funding enabled and organized by Projekt DEAL.

Conflict of Interest

The authors declare no conflict of interest.

Data Availability Statement

The data that support the findings of this study are available from the corresponding author upon reasonable request.

Keywords

diamond, fusion, kinetic inductance detectors, NbN, polarimetry, sapphire

Received: April 27, 2022

Revised: December 9, 2022

Published online:

- [1] A. Monfardini, L. J. Swenson, A. Bideaud, F. X. Désert, S. J. C. Yates, A. Benoit, A. M. Baryshev, J. J. A. Baselmans, S. Doyle, B. Klein, M. Roesch, C. Tucker, P. Ade, M. Calvo, P. Camus, C. Giordano,

- R. Guesten, C. Hoffmann, S. Leclercq, P. Mauskopf, K. F. Schuster, *Astron. Astrophys.* **2010**, 521, A29.
- [2] J. Baselmans, S. J. C. Yates, R. Barends, Y. J. Y. Lankwarden, J. R. Gao, H. Hoevers, T. M. Klapwijk, *J. Low Temp. Phys.* **2008**, 151, 524.
- [3] J. Zmuidzinis, P. L. Richards, *Proc. IEEE* **2004**, 92, 1597.
- [4] D. Marsden, B. A. Mazin, B. Bumble, S. Meeker, K. O'Brien, S. McHugh, M. Strader, E. Langman, in *Proc. SPIE* **2012**, 8453, 84530B.
- [5] F. Mazzocchi, E. Driessen, S. Shu, M. Merker, K. Ilin, M. Siegel, A. Meier, D. Straus, T. Scherer, *IEEE Trans. Appl. Supercond.* **2021**, 31, 2400407.
- [6] M. A. Van Zeeland, R. L. Boivin, D. L. Brower, T. N. Carlstrom, J. A. Chavez, W. X. Ding, R. Feder, D. Johnson, L. Lin, R. C. O'Neill, C. Watts, *Rev. Sci. Instrum.* **2013**, 84, 043501.
- [7] A. J. H. Donné, A. E. Costley, R. Barnsley, H. Bindslev, R. Boivin, G. Conway, R. Fisher, R. Giannella, H. Hartfuss, M. G. von Hellermann, E. Hodgson, L. C. Ingesson, K. Itami, D. Johnson, Y. Kawano, T. Kondoh, A. Krasilnikov, Y. Kusama, A. Litnovsky, P. Lotte, P. Nielsen, T. Nishitani, F. Orsitto, B. J. Peterson, G. Razdobarin, J. Sanchez, M. Sasao, T. Sugie, G. Vayakis, V. Voitsenya, et al., *Nucl. Fusion* **2007**, 47, S337.
- [8] W. Kunz, Equipe TFR *Nucl. Fusion* **1978**, 18, 1729.
- [9] F. Mazzocchi, G. Grossetti, A. Mlynek, E. Poli, D. Strauß, T. Scherer, *Fusion Eng. Des.* **2018**, 130, 1.
- [10] J. Zhang, E. Fretwurst, R. Klanner, H. Perrey, I. Pintilie, T. Poehlsen, J. Schwandt, *J. Instrum.* **2011**, 6, C11013.
- [11] M. Merker, C. Bohn, M. Völlinger, K. Ilin, M. Siegel, *IEEE Trans. Appl. Supercond.* **2017**, 27, 1100205.
- [12] M. Sidorova, A. Semenov, H. W. Hübers, K. Ilin, M. Siegel, I. Charaev, M. Moshkova, N. Kaurova, G. N. Goltsman, X. Zhang, A. Schilling, *Phys. Rev. B* **2020**, 102, 054501.
- [13] S. Doyle, Ph.D. Thesis, Cardiff University **2008**.
- [14] M. Rösch, Ph.D. Thesis, KSP - KIT Scientific Publishing **2014**, Google-Books-ID: y3AcAAQBAJ.
- [15] <https://www.sonnetsoftware.com/support/manuals.asp> (accessed: October 2021).
- [16] S. Shu, Ph.D. Thesis, IRAM, Grenoble **2019**.
- [17] J. Zmuidzinis, *Annu. Rev. Condens. Matter Phys.* **2012**, 3, 169.
- [18] R. A. Khmel'nitsky, A. A. Gippius, *Phase Transitions* **2014**, 87, 175.
- [19] A. J. Annunziata, D. F. Santavicca, L. Frunzio, G. Catelani, M. J. Rooks, A. Frydman, D. E. Prober, *Nanotechnology* **2010**, 21, 445202.
- [20] P. D. Mauskopf, *Publ. Astron. Soc. Pac.* **2018**, 130, 082001.
- [21] A. S. Cooper, *Acta Crystallogr.* **1962**, 15, 578.
- [22] W. M. Yim, R. J. Paff, *J. Appl. Phys.* **1974**, 45, 1456.
- [23] M. E. Straumanis, S. Zyszczyński, *J. Appl. Crystallogr.* **1970**, 3, 1.
- [24] P. W. May, *Endeavour* **1995**, 19, 101.
- [25] H. Yamada, A. Meier, F. Mazzocchi, S. Schreck, T. Scherer, *Diamond Relat. Mater.* **2015**, 58, 1.
- [26] R. Heidinger, G. Dammertz, A. Meier, M. K. Thumm, *IEEE Trans. Plasma Sci.* **2002**, 30, 800.
- [27] O. Noroozian, P. K. Day, B. H. Eom, H. G. Leduc, J. Zmuidzinis, *IEEE Trans. Microwave Theory Tech.* **2012**, 60, 1235.
- [28] S. Wuensch, C. Groetsch, M. Merker, M. Siegel, *IEEE Trans. Appl. Supercond.* **2015**, 25, 2401105.
- [29] A. Adane, G. Coiffard, M. Calvo, J. Goupy, C. Hoarau, S. Leclercq, A. Monfardini, K. F. Schuster, in *2014 11th Int. Workshop on Low Temperature Electronics (WOLTE)*, IEEE, Piscataway, NJ, USA, July **2014**, pp. 81–84.
- [30] S. Shu, M. Calvo, J. Goupy, A. Catalano, A. Bideaud, A. Monfardini, S. Leclercq, E. F. C. Driessen, *IEEE Trans. Terahertz Sci. Technol.* **2018**, 8, 605.
- [31] M. Tinkham, *Introduction to Superconductivity*, Courier Corporation, January **2004**.

- [32] G. Ulbricht, B. A. Mazin, P. Szypryt, A. B. Walter, C. Bockstiegel, B. Bumble, *Appl. Phys. Lett.* **2015**, *106*, 251103.
- [33] G. N. Gol'tsman, B. S. Karasik, O. V. Okunev, A. L. Dzardanov, E. M. Gershenzon, H. Ekstrom, S. Jacobsson, E. Kollberg, *IEEE Trans. Appl. Supercond.* **1995**, *5*, 3065.
- [34] B. Strehl, T. Niinikoski, A. Rijllart, K. Winter, M. Caria, *Phys. Lett. B* **1990**, *242*, 285.
- [35] R. Imazawa, Y. Kawano, T. Akiyama, K. Nakayama, K. Itami, in *Proc. of the 41st Plasma Physics Conf. on Plasma Physics (EPS2014)*, Vol. 5, IOP **2014**, P5.008.
- [36] P. J. de Visser, J. J. A. Baselmans, J. Bueno, N. Llombart, T. M. Klapwijk, *Nat. Commun.* **2014**, *5*, 3130.
- [37] R. Schneider, B. Freitag, D. Gerthsen, K. S. Ilin, M. Siegel, *Cryst. Res. Technol.* **2009**, *44*, 1115.